



# Supercontinuum generation in highly birefringent fiber infiltrated with carbon disulfide

Lanh Chu Van<sup>a</sup>, Bao Tran Le Tran<sup>a</sup>, Trong Dang Van<sup>a</sup>, Ngoc Vo Thi Minh<sup>a</sup>, Thuy Nguyen Thi<sup>b</sup>, Hong Phuong Nguyen Thi<sup>c</sup>, Minh Hang Trang Nguyen<sup>d</sup>, Van Thuy Hoang<sup>a,\*</sup>

<sup>a</sup> Department of Physics, Vinh University, 182 Le Duan, Vinh City, Viet Nam

<sup>b</sup> Hue University of Education, Hue University, 34 Le Loi Street, Hue City, Viet Nam

<sup>c</sup> Nguyen Chi Thanh High School, Hoa Thanh District, Tay Ninh Province, Viet Nam

<sup>d</sup> IGC Tay Ninh High School, Tay Ninh Province, Viet Nam

## ARTICLE INFO

### Keywords:

Optical fiber  
Nonlinear fiber  
Highly birefringent fiber  
Supercontinuum generation  
Polarization  
Coherence  
Negative nonlinear refractive index

## ABSTRACT

Supercontinuum generation in highly birefringent fiber infiltrated with carbon disulfide is numerically studied with a linearly polarized femtosecond laser (1560 nm wavelength, 90 fs pulse duration) as a pump source. The fiber has two polarized modes (x- and y-polarized LP<sub>01</sub>) with different dispersion characteristics, meaning all-normal dispersion for the y-polarized mode and anomalous dispersion for the x-polarized mode. We build a numerical modeling for nonlinear propagation including Kerr effects and Raman effects with positive and negative nonlinear refractive. Our results point out that spectral bandwidth, flatness, and coherence of supercontinuum generation depend on the input polarized angle (an angle with respect to the x-axis) of the laser pulses. In particular, the input pulses polarized near slow-axis (x-axis) provide 1.5 octave-spanning soliton-induced SC generation with bandwidth from 1000 nm to 3300 nm via 10 kW input peak power, while input pulses polarized near the fast-axis (y-axis) create octave-spanning all-normal dispersion supercontinuum generation (from 1200 nm to 2500 nm). Modification of the input angle enables controlling spectro-temporal properties of supercontinuum generation, such as polarization state, coherence, spectral bandwidth, and flatness. In addition, the use of highly birefringent fiber also enables suppression of polarization modulation instability; therefore coherence solely depends on effects of modulation instability and it is possible to tailor via changing the input angle.

## 1. Introduction

Supercontinuum (SC) generation is a well-known technology for paramount applications, such as multiphoton microscopy [1], frequency combs [2], and sensitive bio-sensors [3]. Nowadays, the spectrum of SC sources covers wavelengths ranging from deep UV up to mid-infrared with a watt-level of output power, and high stability [4]. The SC sources, therefore, have motivated applications in, e.g., optical metrology [5,6], spectroscopy [7], and telecommunication [8]. In general, SC generation is induced by using laser pulses with high peak power launched into nonlinear fibers where the nonlinearity and dispersion act simultaneously for spectral broadening and reconfiguring temporal waveforms. Thus, dynamics for the nonlinear propagation process strongly depend on dispersion and nonlinear characteristics of a selected fiber. Classically, fibers with flat, near-zero dispersion have been

popularly used to obtain SC generation with broad spectral bandwidth because phase-matching conditions in such fiber may be set with a further broad wavelength range [9,10]. Besides, development of fiber materials including glasses (e.g., silica, telluride, chalcogenide), liquids, and gases brings about optical fibers with extremely high nonlinearity and broad optical transparency. Consequently, these fibers can provide multi-octave spanning SC generation with uniform spectral profile and high coherence [11–17]. Among the fiber glasses, silica is versatile and popularly used for SC generation because of its high purity, high transparency, strong mechanics, and easy-to-handle for fiber drawing using the stack-and-draw method. However, because of the low nonlinear refractive index, silica-based fibers typically require a high input peak power for broad spanning SC generation (in hundreds of kW), and the spectral broadening is limited at the mid-infrared range (IR) via the high attenuation of silica. Fibers made from soft-glass (non-silica)

\* Corresponding author.

E-mail address: [thuyhv@vinhuni.edu.vn](mailto:thuyhv@vinhuni.edu.vn) (V. Thuy Hoang).

glasses, such as telluride and chalcogenide, have been recently used to generate multi-octave spanning SC with spectral bandwidth spanning from near-IR up to 18  $\mu\text{m}$  [4,18]. Main drawback of the soft-glass fibers relates to their zero-dispersion wavelength (ZDW) which is typically located in the mid-IR range. Thus, a complex pump system with pump wavelength matched with the ZDW (e.g., optical parametric amplifier (OPA), cascade fiber system lasers) is required for SC generation [4,13,18].

Recently, a combination of optical fibers and liquids has been leveraged widely for applications in optofluidics, such as sensors, UV delivery, and supercontinuum [19–23]. Among these applications, liquid core fibers have been studied as an alternative to standard fibers (solid core) for broad SC generation [24–28] via the high nonlinearity and high transparency of selected liquids. For example, carbon disulfide ( $\text{CS}_2$ ), and carbon tetrachloride ( $\text{CCl}_4$ ) have high transparency from the visible range up to mid-IR [27,29].  $\text{CS}_2$  has a high nonlinear refractive index comparable to one of the soft glasses [30] and its nonlinear refractive index strongly depends on pulse duration of excited lasers, such as  $\text{CS}_2$  has  $3 \times 10^{-19} \text{ m}^2/\text{W}$  with ultra-short laser pulses ( $<100 \text{ fs}$ ) and up to  $20 \times 10^{-19} \text{ m}^2/\text{W}$  with picosecond laser pulses [30]. Moreover, sensitivity of optical properties of selected liquids via changing temperature and pressure allows readily controlling properties of liquid core fibers, and thus, “on the fly” customizes spectro-temporal properties of SC generation [31].

Nonlinear refractive index of  $\text{CS}_2$  consists of bound-electronic nonlinear parts (e.g., instantaneous Kerr effects)  $n_{2el}$  and molecular effects  $n_{2m}$  (non-instantaneous effects) [30,32]. The bound-electronic nonlinear part has a response time of around 1 fs, which is essentially instantaneous compared to laser pulse duration (hundreds of femtoseconds). The sign and value of instantaneous nonlinearity do not efficiently depend on the polarization of input laser pulses [30,32,33]. Whilst, interestingly, non-instantaneous nonlinearity originated from molecular effects (e.g., reorientation, libration) strongly depends on the polarization angle between “pump” and “probe” lasers [30,32,33]. For instance, the “probe” laser beam with linear polarization perpendicular (or parallel) to that of the “pump” may experience nonlinear dynamics with negative (or positive) values of non-instantaneous nonlinearity [30,32,33]. This interesting property paves a promising approach to readily adjust the dynamics of nonlinear propagation via changing the polarization angle of the “pump–probe” laser configuration for various applications, such as optical pulse compressors with normal dispersion fibers [34]. Herein, we leverage the interesting properties of  $\text{CS}_2$  to yield SC generation with a broad spectral bandwidth and high coherence.

It is worth mentioning that the coherence of SC generation depends on the effects of input noises, such as vacuum noise, and spontaneous Raman scattering (SRS) [35,36]. These noises are the main seeds for spectral broadening (i.e., noise-driven SC generation) if long pulse lasers (i.e., nanosecond or continuous wave (CW) lasers) are used as pump sources. However, SC generation in such a case does not exhibit coherence. For sub-picosecond laser pulses, nonlinear dynamics of SC generation and the coherence depend on the regime of the dispersion. SC generation in anomalous dispersion is created by soliton dynamics, e.g., soliton fission, soliton shifting, and dispersive wave (DW). Notable features of soliton-induced SC generation are spectrum and spectrogram with complex structures [35]. Moreover, soliton-induced SC also exhibits low coherence via effects of vacuum noises amplified by modulation instability (MI). In contrast, MI is suppressed in a normal dispersion regime, and thus, all-normal dispersion (ANDi) SC generation typically has high coherence. Notwithstanding, a drawback of ANDi SC generation is to require a much higher input peak power of laser pulses than soliton-induced SC generation.

Coherence also significantly depends on the technical noises (i.e., polarization noise, laser noise [37–39]). The laser noise is a fluctuation of amplitude and duration of each laser pulse compared to the mean one resulting in instability of output SC spectrum. Effects of laser noise can be significantly mitigated with the use of short pulse duration and/or

short fiber samples. Meanwhile, polarization noise (i.e., vacuum noise amplified by polarization MI) is a significant effect to degrade coherence in both anomalous and normal dispersion [37,38]. The effect of polarization noise depends on the pulse duration, fiber length, and birefringence of the fiber. In the low birefringence fiber, polarization MI (PMI) results in degradation of the coherence with the use of high input peak power and/or long-duration laser pulses. However, PMI only occurs when the phase-matching condition is set by dispersion, birefringence, and peak power. Therefore, high birefringence fibers with all-normal dispersion have been developed to improve the coherence [40–42]. For example, ANDi SC generation is numerically simulated in a polarization-maintaining liquid core photonic crystal fiber (PCF) [40] with 0.82 octave-spanning (from 1.32  $\mu\text{m}$  to 2.33  $\mu\text{m}$ ). However, the proposed fiber shown in ref. [40] has used ethanol to fill into two air holes in the cladding for significantly asymmetrical distribution of the cladding refractive index (between the fast- and slow-axis), this leads to hard loading work for selectively liquid infiltration if the fiber is fabricated.

In this work, we numerically simulate SC generation in highly birefringent liquid core fibers, in which the core is infiltrated with carbon disulfide to improve the nonlinear coefficient and optical transparency. In particular, we propose a fiber structure made from silica and germanium-doped silica that provides high birefringence in the near-infrared range. Next, we characterize the properties of SC generation (e.g., polarization state, coherence, spectral bandwidth) with the varying input polarized angle. For the first time, the effects of polarization noise, as well as the coupling between the polarized modes in a highly birefringent liquid core fiber, are thoroughly numerically studied. We pointed out that the coherence of SC generation in the fiber depends on the angle of the input pulses with the slow axis (x-axis).  $\text{CS}_2$  is selected to infiltrate into the core because it has a higher nonlinear refractive index compared to other liquids [32], and high transparency.

## 2. Fiber development

In general, highly birefringent fibers have an asymmetrical structure and/or asymmetrical profile of refractive index. As shown in Fig. 1 (a), the structure of the proposed fibers is configured from a “panda” shape on the x-axis, a bow-tie shape on the y-axis, and the central air-hole is infiltrated with  $\text{CS}_2$ . It is worth mentioning that liquids do not experience any photoelasticity stress that causes stress-induced birefringence. For the proposed fiber configuration, high birefringence between the x- and the y-axis is induced by the refractive index difference of the selected materials on the bow-tie and “panda” parts. Here, the selected materials are air and germanium (Ge)-doped silica.

Linear properties of the proposed fibers (e.g., dispersion, mode area) are calculated using the full-vectorial finite-difference with a perfectly matched layer (PML). The calculated region is rectangular with a size of  $10 \times 10 \mu\text{m}$  to cover the whole fiber structure (i.e., the core, two cladding air-holes, and Ge-doped bow-tie part). The size of a mesh point is  $0.02 \mu\text{m}$ .

Ratio between diameter of the air-holes ( $d_1$ ) and core ( $d_c$ ) is kept constant at 1.5. The two air holes in the x-axis have a larger diameter than the core to make a high contrast of refractive index between the x- and the y-axis for high birefringence, and also for reduction of confinement loss. The strand thickness between the air holes and the liquid core (as well as between the bow-tie and liquid core) is kept constant at 200 nm to ensure the technological feasibility of fiber fabrication. The bow-tie parts are Ge-doped silica with a mol concentration of 20 %. In reality, it has been experimentally investigated Ge-doped silica fiber with a concentration of up to 90 % [43,44]. However, high Ge concentration leads to a decrease in the contrast of refractive index between the core and cladding, this causes an increase in confinement loss in a long wavelength range, especially for the x-polarized mode. For fiber with  $d_c = 2.4 \mu\text{m}$ , ratio of the leaky energy (in the cladding region) and light confined inside the core - for the y-and the

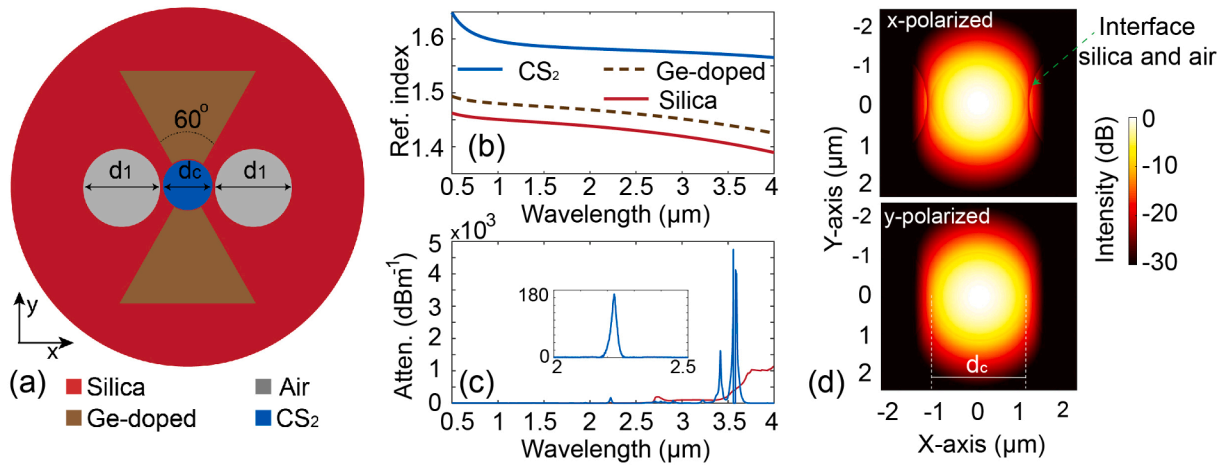


Fig. 1. (a) Schematic structure of the highly birefringent fiber, (b) refractive index of CS<sub>2</sub> [49] and 20 % Ge-doped silica, and silica [50], (c) attenuation of CS<sub>2</sub> [27,29] and silica [51], and (d) electrical energy distribution of the x- and the y-polarized LP<sub>01</sub> mode of 20 % Ge-doped fiber with a core diameter of 2.4 μm and wavelength at 1560 nm.

x-polarized modes, respectively - is 4 % and 6 % for 20 % Ge-doped fiber and 6 % and 8 % for 40 % Ge-doped fiber.

Asymmetry of the refractive index profile causes the difference in electromagnetic distribution between x- and y- polarized modes. For example, Fig. 1 (d) presents the electrical energy distribution (at λ = 1560 nm) of the x- and y-polarized LP<sub>01</sub> mode for 20 % Ge-doped fiber with d<sub>c</sub> = 2.4 μm, in which the traces of light refraction and reflection at the interface between silica and air are sharply visible for the x-polarized mode.

From the experimental perspective, the proposed fiber is possible to fabricate using the stack-and-draw method [45,46], and the method for selective liquid infiltration [47,48].

Refractive index and attenuation of silica and CS<sub>2</sub> as shown in Fig. 1 (c-d) are used to calculate linear properties of the proposed fiber. Material attenuation of Ge-doped silica is assumed to be similar to that of silica. CS<sub>2</sub> has a peak attenuation (162 dB/m) at 2.2 μm and high attenuation around 3.5 μm, whilst silica has high attenuation in the mid-IR range.

Refractive index of Ge-doped silica is calculated according to Eq. (1) [50], where X is mol concentration (%), BS<sub>i</sub> and CS<sub>i</sub> are Sellmeier coefficients of silica, BG<sub>i</sub> and CG<sub>i</sub> are Sellmeier coefficients of GeO<sub>2</sub>. Sellmeier coefficients of these materials are shown in Table 1.

$$n = \sqrt{1 + \sum_{i=1}^3 \frac{[BS_i + X(BG_i - BS_i)\lambda^2]}{\lambda^2 - [CS_i + X(CG_i - CS_i)]^2}} \quad (1)$$

Dispersion characteristics of the fibers with various values of core diameter are shown in Fig. 2. The fiber with a small core diameter (d<sub>c</sub> = 2 μm) has all-normal dispersion in the investigated wavelength range for both x- and y-polarized modes. The increase in core diameter leads to shifting of the dispersion toward the anomalous regime. It is also worth noting that dispersion characteristics also depend on the contrast of the refractive index of the core and cladding. Therefore, the x-polarized mode has a dispersion noticeably different from one of the y-polarized

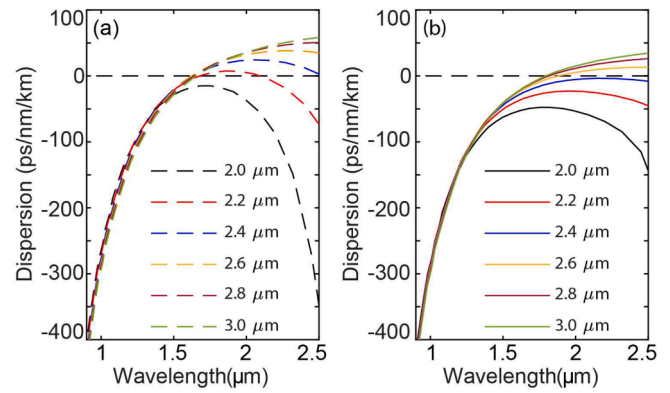


Fig. 2. Dispersion characteristics of birefringent fiber with various core diameters. (a) x-polarized mode, (b) y-polarized mode.

mode in short-wavelength infrared (SWIR) (λ > 1500 nm). For a given value of core diameter, the x-polarized mode has a dispersion profile shifted toward an anomalous regime compared to that of the y-polarized mode.

The spectral bandwidth of SC generation critically depends on dispersion characteristics of a selected fiber. For instance, a fiber with flat, near-zero dispersion can provide further broad bandwidth SC spectra than that generated in fiber with high slope dispersion. Among the investigated fiber structures, the fibers with a small core (d<sub>c</sub> = 2 and 2.2 μm) have a dispersion shape with a large slope in the near-IR range resulting in a limitation of spectral broadening. The large core fibers (d<sub>c</sub> = 2.6–3 μm) have anomalous dispersion in the near-IR range for both x- and y-polarized modes. Therefore, these fibers are not an appropriate choice for flat-top, high coherence SC generation. The fiber with d<sub>c</sub> = 2.4 μm has a flat, all-normal dispersion for the y-polarized mode and anomalous dispersion for the x-polarized mode. This fiber may offer either ANDi or soliton-induced SC generation that depends on the angle between the input pulse and the x-axis. In the following sections, properties of SC generation in this fiber would be considered.

Linear properties of the proposed fiber are presented in Fig. 3 (a-d). The y-polarized mode has normal dispersion in near and mid-IR range and zero-dispersion wavelength (ZDW) at 3800 nm, while the x-polarized mode has three ZDWs at 1520 nm (λ<sub>D1</sub>), 2480 nm (ZDW<sub>2</sub>) and 3400 nm (ZDW<sub>3</sub>). Both x-polarized and y-polarized have flat, near-zero dispersion in the wavelength range of 1500 nm – 3000 nm, where the maximum values of dispersion are 26.5 (ps/nm/km) at 1940 nm for the

Table 1  
Sellmeier coefficients of CS<sub>2</sub>, GeO<sub>2</sub>, and silica.

Coef.	CS <sub>2</sub> [49]	GeO <sub>2</sub> [52]	Silica [50]
B1	1.499426	0.80686642	0.6961663
B2	0.089531	0.71815848	0.4079426
B3	0	0.85416831	0.8974794
C1 (μm <sup>2</sup> )	0.178763	0.068972606	0.0684043
C2 (μm <sup>2</sup> )	6.591946	0.15396605	0.1162414
C3 (μm <sup>2</sup> )	0	11.841931	9.896161

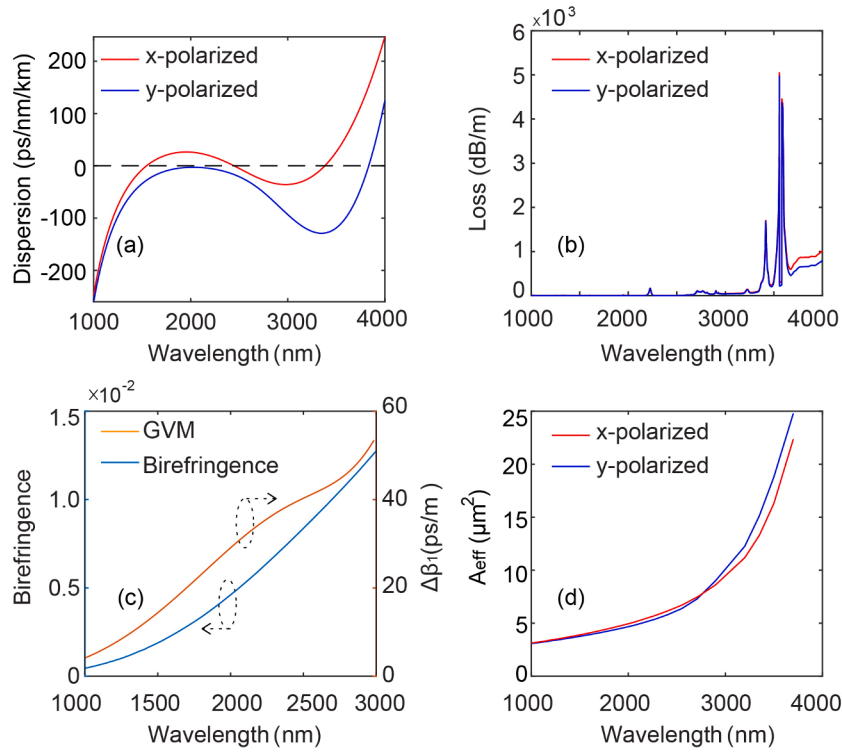


Fig. 3. Linear properties of the fundamental mode in proposed fiber. (a) dispersion shapes, (b) loss, (c) phase birefringent and group velocity mismatch, and (d) effective mode area.

x-polarized mode and  $-13$  (ps/nm/km) at  $2390$  nm for y-polarized mode. The effective area ( $A_{eff}$ ) of the modes varies from  $3$  to  $25 \mu\text{m}^2$  in a wavelength range of  $1000$ – $3800$  nm.

$\text{CS}_2$  has higher refractive index than that of silica, thus the light can be strongly confined inside the core resulting in low confinement losses. Loss of the proposed fiber is approximate to a sum of the confinement loss and material attenuation of  $\text{CS}_2$  in the core, silica, and Ge-doped in the cladding. The fiber loss is estimated by using the full-vectorial finite-difference method with a  $100 \times 100 \mu\text{m}$  calculated rectangular region. As shown in Fig. 3 (b), the fiber loss follows the material attenuation profile of  $\text{CS}_2$  with a peak of loss at  $2.2 \mu\text{m}$ , and extremely high loss at long wavelength ( $\lambda > 3.3 \mu\text{m}$ ), limiting the spectral broadening in the mid-IR range.

The phase birefringence and the group velocity mismatch (GVM) are determined by Eq. (2) and Eq. (3):

$$B = n_{effy} - n_{effx} \quad (2)$$

$$\Delta\beta_1 = v_{gx}^{-1} - v_{gy}^{-1} \quad (3)$$

where  $n_{effy}$  and  $n_{effx}$  are effective refractive index,  $v_{gx}$  and  $v_{gy}$  are group velocities of x- and y-polarized modes, respectively.

The value of  $B$  varies in a range of  $0.05 \times 10^{-2}$ – $1.2 \times 10^{-2}$  in the wavelength range of  $1$ – $3 \mu\text{m}$ , and it is one or two orders of magnitude higher than that of standard birefringence fibers (around  $6 \times 10^{-4}$ ). The group velocity mismatch varies in a range of  $4.5$  (ps/m) –  $50$  (ps/m).

### 3. Numerical modelling

Nonlinearity of  $\text{CS}_2$  originates from reaction of bound electrons and molecules via effects of an external electromagnetic (EM) field. In context of Born–Oppenheimer approximation, bound-electronic and molecular dynamics contribute separately to nonlinearity of  $\text{CS}_2$  so that third-order susceptibility is a sum of bound-electronic and molecular parts as given in Eq. (4) [33,53]:

$$\chi_{ijkl}^{(3)} = \chi_{ijkl}^{(3,el)} + d(t)_{ijkl}^{(3,m)} \quad (4)$$

where  $\chi_{ijkl}^{(3,el)}$  and  $d_{ijkl}^{(3,m)}$  are third-order susceptibility of bound-electronic and molecular nonlinearity, respectively, as given in Eq. (5) [54]:

$$\begin{aligned} \chi_{ijkl}^{(3,el)} &= \chi_{xxyy}^{(3,el)} \delta_{ij} \delta_{kl} + \chi_{xyxy}^{(3,el)} \delta_{ik} \delta_{jl} + \chi_{xyyx}^{(3,el)} \delta_{il} \delta_{jk} \\ d_{ijkl}^{(3,m)}(t) &= a(t) \delta_{ij} \delta_{kl} + \frac{1}{2} b(t) \delta_{ik} \delta_{jl} + \frac{1}{2} b(t) \delta_{il} \delta_{jk} + c(t) \delta_{ijkl} \end{aligned} \quad (5)$$

It is to note that  $c(t) = 0$  for isotropic materials. However,  $\text{CS}_2$  in the core of the proposed fiber exhibits as an anisotropic material via effects of polarization of external EM field (i.e., nonlinearity on x- and y-direction may be different from each other), resulting in  $c(t) \neq 0$ .

In this context, x- and y-component of the nonlinear polarization are given in Eq. (6) [54]:

$$\begin{aligned} P_i &= \sum_j \left[ \left( \frac{3\epsilon_0}{4} \chi_{xxyy}^{(3,el)} + a(t) \right) E_i E_j E_j^* + \left( \frac{3\epsilon_0}{4} \chi_{xyxy}^{(3,el)} + \frac{1}{2} b(t) \right) E_j E_i E_j^* \right. \\ &\quad \left. + \left( \frac{3\epsilon_0}{4} \chi_{xyyx}^{(3,el)} + \frac{1}{2} b(t) \right) E_j E_j E_i^* + c(t) E_i E_j E_j^* \right] \end{aligned} \quad (6)$$

where  $i, j = x$  or  $y$ .

We assume that: (i) the instantaneous nonlinearity (e.g., bound-electronic nonlinearity) does not depend on the polarization of pump laser pulses; and (ii) the three components of third-order susceptibility for bound-electronic nonlinearity have nearly the same magnitude, i.e.,  $\chi_{xxyy}^{(3,el)} = \chi_{xyxy}^{(3,el)} = \chi_{xyyx}^{(3,el)} = \chi_{xxxx}^{(3,el)}/3$  [30,54]. Therefore, Eq. (6) is rewritten as below:

$$\begin{aligned} P_x &= \frac{3\epsilon_0}{4} \chi_{xxxx}^{(3,el)} \left[ \left( |E_x|^2 + \frac{2}{3} |E_y|^2 \right) E_x + \frac{1}{3} (E_x^* E_y) E_y \right] + \left[ h \parallel |E_x|^2 E_x \right. \\ &\quad \left. + h_{\perp} |E_y|^2 E_x + \frac{1}{2} b(t) (E_x^* E_y) E_y \right] \end{aligned} \quad (7)$$

$$P_y = \frac{3\epsilon_0}{4} \chi_{xxxx}^{(3,el)} \left[ \left( |E_y|^2 + \frac{2}{3} |E_x|^2 \right) E_y + \frac{1}{3} \left( E_y^* E_x \right) E_x \right] + \left[ h_{\parallel} |E_y|^2 E_y + h_{\perp} |E_x|^2 E_y + \frac{1}{2} b(t) \left( E_y^* E_x \right) E_x \right] \quad (8)$$

where  $h_{\parallel} = a(t) + b(t) + c(t)$  and  $h_{\perp} = a(t) + \frac{1}{2} b(t)$ .

Relying on Eq. (7) and (8), the coupled general nonlinear Schrödinger equations (GNLSE) for nonlinear propagation in the proposed fiber is given in Eq. (9):

$$\begin{aligned} & \frac{\partial A_{x,y}}{\partial z} + \frac{\alpha_{x,y}}{2} A_y + \Delta\beta_{1x,y} \frac{\partial A_{x,y}}{\partial T} - \sum_{k \geq 2} \frac{i^{k+1}}{k!} \beta_k^{x,y} \frac{\partial^k A_{x,y}}{\partial T^k} = i\gamma \left( 1 + i\tau_{shock} \frac{\partial}{\partial T} \right) \times \\ & \left\{ (1 - f_R) \left( |A_{x,y}|^2 + \frac{2}{3} |A_{y,x}|^2 \right) A_{x,y} + f_R A_{x,y} \left[ \int h_{\parallel}(T - T') |A_{x,y}(T - T')|^2 dT' + \int h_{\perp}(T - T') |A_{y,x}(T - T')|^2 dT' \right] \right\} \\ & + i\gamma \exp(\pm 2i\Delta\beta_0 z) \left[ \frac{1}{3} (1 - f_R) A_{x,y}^* A_{y,x}^2 + \frac{1}{2} f_R \int b(T - T') A_{x,y}^* A_{y,x}^2 dT' \right] \end{aligned} \quad (9)$$

where  $A_{x,y}$  are x-axis and y-axis amplitude,  $T$  is the retarded time frame comoving with  $A_y$  given by  $T = t - z/v_{g,y}$ , group velocity mismatch that is  $\Delta\beta_{1x} = \Delta\beta_1$  for  $A_x$  and  $\Delta\beta_{1y} = 0$  for  $A_y$ . The derivative term of  $T$  in Eq. (9) presents the effect of self-steepening, optical shock formation with  $\tau_{shock} = 1/\omega_0$  ( $\omega_0$  is frequency of pump wavelength). Nonlinear coefficient  $\gamma$  is determined by effective mode area and nonlinear refractive index of CS<sub>2</sub> as given in Eq. (10) where  $n_2$  is where the nonlinear refractive index of CS<sub>2</sub>:

$$\gamma = \frac{2\pi n_2}{\lambda A_{eff}} \quad (10)$$

The proposed fiber with large birefringence, for example,  $B = 2 \times 10^3$ ,  $L_B \approx 0.8$  mm,  $\Delta\beta_0 = 7.8 \times 10^3$  (m<sup>-1</sup>) at a pump wavelength of 1560 nm. Therefore, the exponential factors in the last term of Eq. (9) oscillate rapidly and change the sign rapidly, consequently their constitution averages out to zero [54]. In this context, the last term in Eq. (9) is neglected, and a model of nonlinear propagation inside the proposed fiber is given in Eq. (11):

$$\begin{aligned} & \frac{\partial A_{x,y}}{\partial z} + \frac{\alpha_{x,y}}{2} A_y + \Delta\beta_{1x,y} \frac{\partial A_{x,y}}{\partial T} - \sum_{k \geq 2} \frac{i^{k+1}}{k!} \beta_k^{x,y} \frac{\partial^k A_{x,y}}{\partial T^k} = i\gamma \left( 1 + i\tau_{shock} \frac{\partial}{\partial T} \right) \times \\ & \left\{ (1 - f_R) \left( |A_{x,y}|^2 + \frac{2}{3} |A_{y,x}|^2 \right) A_{x,y} + f_R A_{x,y} \left[ \int h_{\parallel}(T - T') |A_{x,y}(T - T')|^2 dT' + \int h_{\perp}(T - T') |A_{y,x}(T - T')|^2 dT' \right] \right\} \end{aligned} \quad (11)$$

The parallel and perpendicular Raman functions (i.e.,  $h_{\parallel}(T)$  and  $h_{\perp}(T)$ ) are determined by previous works [32,34], as given in Eq. (12–13):

$$h_{\parallel}(T) = \frac{1}{N_{2\parallel}} \left( n_{2\parallel} e^{-T/\tau_{l,j}} \int_0^{\infty} \frac{\sin(\omega T)}{\omega} g(\omega) d\omega + \sum_{k=c,d} n_{2k\parallel} \left( 1 - e^{-T/\tau_{l,k}} \right) e^{-T/\tau_{l,k}} \right) \quad (12)$$

$$h_{\perp}(T) = \frac{1}{N_{2\perp}} \sum_{i=d,l} \left[ n_{2i\perp} \frac{1}{t_{i\perp}^2 - t_{\perp 0}} \left( \exp\left(-\frac{T}{t_{i\perp}}\right) - \exp\left(-\frac{T}{t_{\perp 0}}\right) \right) \right] \quad (13)$$

where  $g(\omega)$  is distribution function of librational motion as shown in Eq.

(14) [32].

$$g(\omega) = e^{\left( \frac{-(\omega - \omega_0)^3}{2\sigma^2} \right)} - e^{\left( \frac{-(\omega + \omega_0)^3}{2\sigma^2} \right)} \quad (14)$$

The subscripts  $d, l, c$  indicate the molecular reorientation, molecular interaction, and collision-induced, respectively. The collision-induced is isotropic symmetry (i.e., independent of the polarization) [30]. The subscript  $l$  in Eq. (13) indicates intermolecular interaction including molecular interaction and collision-induced [34].  $N_{2\parallel} = n_{2d\parallel} + n_{2l\parallel} + n_{2c\parallel}$

and  $N_{2\perp} = |n_{2d\perp}| + |n_{2l\perp}|$ . Values of nonlinear parameters of CS<sub>2</sub> are shown in Table 2.

For femtosecond laser pulses with a pulse duration of 90 fs, CS<sub>2</sub> has a nonlinear refractive index is around of  $3 \times 10^{-19}$  m<sup>2</sup>/W, and Raman fraction ( $f_R$ ) is 0.5 [30,32], and these values are assumed to apply for both polarized modes of the proposed fiber.

Coherence characteristics of SC generation in the proposed fiber are numerically calculated using the first-order coherence in the form [35] as given in Eq. (15) for the x- and the y-components separately:

$$|g_{12-x,y}^{(1)}(\omega)| = \left| \frac{\left\langle \tilde{A}_{i-x,y}^* (\omega) \tilde{A}_{j-x,y}(\omega) \right\rangle_{i \neq j}}{\left[ \left\langle \left| \tilde{A}_{i-x,y}(\omega) \right|^2 \right\rangle \left\langle \left| \tilde{A}_{j-x,y}(\omega) \right|^2 \right\rangle \right]^{1/2}} \right| \quad (15)$$

The vacuum noise (shot noise) is taken into account in our model to characterize the coherence of SC generation in which the shot noise is performed by the addition of one photon with a random phase per each

**Table 2**

Values of nonlinear parameters of CS<sub>2</sub> responses to parallel and perpendicular polarization [32,34].

Parameters	Values	Parameters	Values
$n_{2d\parallel}$ (10 <sup>-19</sup> m <sup>2</sup> /W)	18	$n_{2d\perp}$	-9.44
$n_{2l\parallel}$ (10 <sup>-19</sup> m <sup>2</sup> /W)	7.6	$n_{2l\perp}$	-3.73
$n_{2c\parallel}$ (10 <sup>-19</sup> m <sup>2</sup> /W)	1.0	$t_{\perp 0}$ (ps)	0.1
$\tau_{r,d}$ (ps)	0.15	$t_{\perp}^d$ (ps)	0.107
$\tau_{r,c}$ (ps)	1.61	$t_{\perp}^c$ (ps)	1.281
$\tau_{r,e}$ (ps)	0.15	$\gamma$ with 90 fs (W <sup>-1</sup> km <sup>-1</sup> ) at 1560 nm	350
$\tau_{f,c}$ (ps)	0.14	$f_R$ with 90 fs	0.5
$\tau_{f,l}$ (ps)	0.45	$n_{2,eff}$ with 90 fs (10 <sup>-19</sup> m <sup>2</sup> /W)	3
$\omega_0$ (ps <sup>-1</sup> )	8.5	$N_{2\parallel}$ (10 <sup>-19</sup> m <sup>2</sup> /W)	26.6
$\sigma$ (ps <sup>-1</sup> )	5	$N_{2\perp}$ (10 <sup>-19</sup> m <sup>2</sup> /W)	13.17

simulation bin [35]. We do not consider the effects of pulse-to-pulse relative intensity noise (RIN) (i.e., the fluctuation of the amplitude and duration of individual laser pulses compared to the mean value) on the degradation of the coherence [39] because RIN is expected to have only minor effects on the coherence with a short fiber sample and short laser pulses [39,55]. The coherence is calculated from 20 simulations with random values of input noises resulting in 190 unique pairs. The average value  $\langle |g_{12}^{(1)}| \rangle$  is an arithmetic mean of the coherence over the investigated wavelength range.

Ellipticity as shown in Eq. (16) is used to determine the polarization state at every wavelength bit of the SC spectrum [37].

$$e_p = \frac{2Im\left(\tilde{A}_x(\omega)\tilde{A}_y^*(\omega)\right)}{\left|\tilde{A}_x(\omega)\right|^2 + \left|\tilde{A}_y(\omega)\right|^2} \quad (16)$$

The input pulses follow the Gaussian temporal profile given by Eq. (17–18):

$$A(0, T) = \sqrt{P_0} \exp\left(-2\ln(2)\left(\frac{T}{T_0}\right)^2\right) \quad (17)$$

$$A_x(0, T) = A(0, T)\cos(\theta) \text{ and } A_y(0, T) = A(0, T)\sin(\theta)$$

where  $T_0$  is the pulse duration (full width at half maximum -FWHM),  $\theta$  is an angle with respect to the x-axis of the linear polarized input pulse.

The parameters from a low cost, linear polarization maintaining, available commercial femtosecond laser with central wavelength at 1560 nm, and pulse duration of 90 fs (e.g., Femtosecond Erbium Laser of MENLO Inc.) are used as a pump source to thoroughly study SC generation in the proposed fiber. Although CS<sub>2</sub> has a lower nonlinear refractive index pumped by a short pulse laser than that induced by a long pulse laser (e.g., a picosecond laser), the use of a short pulse laser typically sets up SC generation with further high coherence [38,39].

## 4. Results and discussion

### 4.1. x- and y-polarized input pulse

When the input pulse is linearly polarized along the x-axis (an angle with respect to the x-axis  $\theta \approx 0^\circ$ ), the soliton dynamics are dominant to generate the x-polarized SC generation. Fiber length is 10 cm and the input peak power  $P_0$  is 10 kW. Intensity of the y-component is at the noise level, and the polarization state also does not change covering the whole of the spectrum, Fig. 4 (c-d). Therefore, only MI is assumed to

have dominant effects to amplify the noise resulting in a degradation of coherence, whilst effects of PMI are ignored.

The dynamics for pulse broadening during propagation is presented in Fig. 4 with SPM at the beginning of the propagation, followed by soliton fission and DW. The positive slope of dispersion at ZDW<sub>1</sub> and ZDW<sub>3</sub> as well as the negative slope of dispersion at ZDW<sub>2</sub> leads to blue-shifting and red-shifting DW to create new wavelengths in the normal dispersion regime. The direct soliton spectrum tunneling (DSST) contributes to creating wavelength in the anomalous dispersion regime with wavelengths longer than ZDW<sub>3</sub> [56]. Consequently, the x-polarized SC generation has a two-octave spanning spectral bandwidth (1000 nm – 4000 nm) in the short length of propagation from the offset (around 1.5 cm), Fig. 4 (b). However, CS<sub>2</sub> absorbs strongly the light at the mid-IR range ( $\lambda > 3.3 \mu\text{m}$ ), therefore the spectrum at 10 cm of propagation spans only 1.5-octave bandwidth (1000–3300 nm) within 40 dB, Fig. 4 (b-c).

It is to note that x-polarized mode has lower group velocity than that of the y-mode, thus x-components of SC generation have further delay compared to those on the y-axis. The delay of x-components is presented in Fig. 4 (a), in which the spectrogram tends to shift towards the right side.

In order to determine the nonlinear properties of the fiber, characteristic lengths of pulse broadening dynamics in the investigated fiber are calculated, using the following set of formulas:

$$L_D = \frac{T_0^2}{|\beta_2|}, L_{NL} = \frac{1}{\gamma P_0}, N = \sqrt{\frac{L_D}{L_{NL}}}, L_{fiss} \approx \frac{L_D}{N}, L_{MI} \approx 16L_{NL} \quad (19)$$

where  $L_D$ ,  $L_{NL}$ ,  $L_{fiss}$ ,  $L_{MI}$  are dispersion, nonlinear, soliton fission, and modulation instability characteristics length, respectively.  $N$  is the soliton number.  $P_0$  and  $T_0$  are the peak power and pulse duration of an input pulse.

For input peak power of 10 kW, soliton number  $N \approx 70$ ,  $L_{MI} = 0.4$  cm,  $L_{fiss} = 1.9$  cm. The MI length is much shorter than one of the soliton fission length, it means that MI can significantly amplify the vacuum noise before soliton fission occurs. Thus, the coherence of the SC generation is significantly reduced with the average coherence  $\langle |g_{12}^{(1)}| \rangle = 0.5$ , Fig. 4 (c).

Fig. 5 presents y-polarized SC generation when input pulses are polarized along the y-axis ( $\theta \approx 90^\circ$ ). SC generation on the y-axis is created by typically nonlinear dynamics for ANDi SC, such as self-phase modulation (SPM), and optical wave breaking (OWB). Meanwhile, the x-axis component is at noise level and it does not influence the properties of SC generation, Fig. 5 (c).

SPM occurs at the beginning of propagation to create new spectral components around the pump wavelength. The most notable feature is

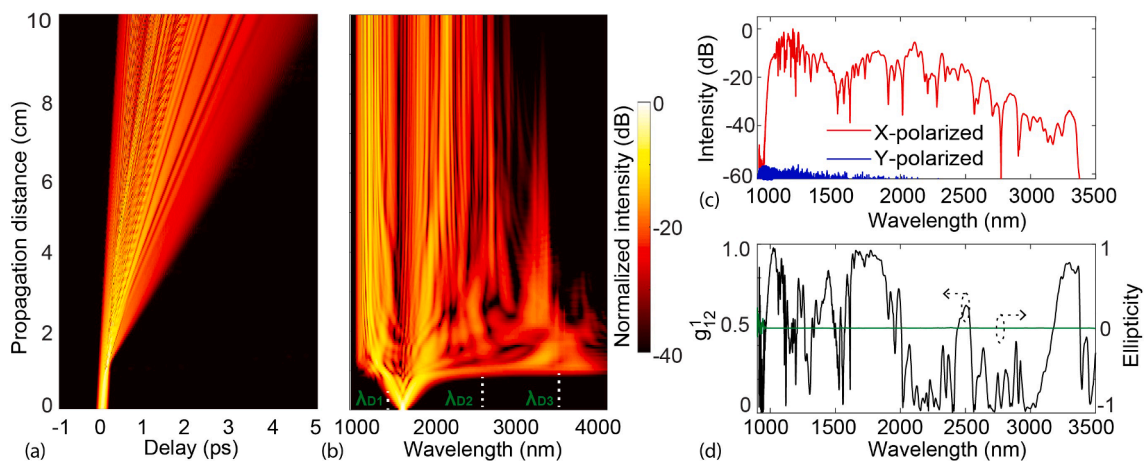


Fig. 4. SC generation with input pulses polarized along the x-axis. (a) evolution of temporal profile, (b) evolution of spectral broadening, (c) spectrum of x- and y-components at 10 cm of propagation, and (d) coherence and ellipticity of the SC spectrum.

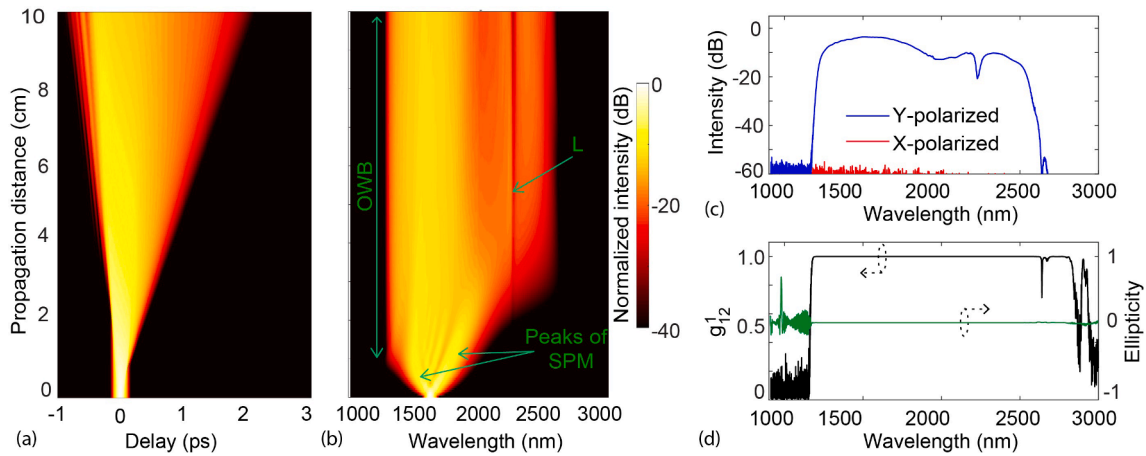


Fig. 5. SC generation with input pulses polarized along the y-axis. (a) evolution on temporal profile, (b) evolution of spectral intensity, (c) spectrum of x- and y-components at 10 cm of propagation, and (d) coherence and ellipticity of the SC spectrum.

that the SPM-induced spectrum consists of many peaks covering the entire wavelength range, and the outermost spectral peaks have the highest relative intensity. The SPM-induced spectrum experiences the dispersion effects of the fiber during further propagation. Particularly, in the normal dispersion regime, the blue-shifted wavelengths at the trailing edge move slower than the components in the forward pulse tail. Consequently, the temporal overlap between blue-shifted and the pulse tails may create new wavelengths via four-wave mixing (FWM), such as new wavelengths around 1200 nm at 1 cm propagation distance on the trailing edge, Fig. 5 (b). Such FWM-induced wavelength is attributed to OWB. At the leading edge, OWB occurs around 4 cm of propagation and creates wavelengths around 2500 nm. It is to note that FWM creating the new wavelength at the edges only occurs when the pump temporally overlaps with the seed. This leads to no new wavelength being generated during further propagation. However, FWM causes the energy redistributed from the center of the pulse to the spectral sidelobes, which makes the SC get further smooth. For peak power of 10 kW, ANDi SCG has spectral bandwidth in a range of 1200–2500 nm with 20 dB dynamics. The trace (L) in Fig. 5 (b) shows a decrease of spectral SC intensity induced by peak of CS<sub>2</sub> attenuation at 2.2 μm. The temporal profiles are only stretched out due to the effects of dispersion effects, Fig. 5 (a).

MI is suppressed in an all-normal dispersion regime resulting in improvement of the coherence. Besides, the x-component is at level noise and extremely lower than the y-components. The low intensity of the x-component points out that there is no coupling between the polarized modes via the effects of PMI. Because of this, the y-polarized

SC spectrum has high coherence and the polarization does not change (i. e.,  $e_p = 0$ ) at every wavelength bit of the SC spectrum, Fig. 5 (d).

#### 4.2. Input orientation angle

When the input pulse is aligned along a non-zero angle with the x and/or the y-axis ( $\theta \neq 0^\circ$  and  $90^\circ$ ), such input pulse is coupled into both x- and y- polarized modes. Thus, there are ANDi and soliton-induced SC generation occurring in the y- and the x-axis at the same time.

Fig. 6 presents evolution of input pulses on x- and y- axis with various input angles. When the input pulse is aligned far from the y-axis (e.g.,  $\theta < 80^\circ$ ), nonlinear interaction (e.g., cross-phase modulation) between the x- and y-mode leads to complex structures of normal-dispersion SC on the y-axis, Fig. 6 (a,b). When the input pulses are aligned close to the y-axis, the intensity on the x-axis is much lower than those on the y-axis, and the pulse evolution on the y-axis is mainly induced by the ANDi nonlinear dynamics, Fig. 6 (c). The effects of x-components on the pulse evolution of y-components can be ignored.

The temporal and spectral profiles at 10 cm of propagation for various input angles are presented in Fig. 7. If an input pulse is polarized near the x-axis, for example,  $\theta = 10^\circ$  as shown in Fig. 7 (b). The soliton-induced SC generation on the x-axis is dominant with spectral bandwidth from 1000 to 3300 nm, while the y-component is not significantly broadening. The coherence of x-components, therefore, is low with  $\langle g_{12}^2 \rangle = 0.5$  as a result of vacuum noise effects. The increase of  $\theta$  leads to reduction of input light energy coupled to the x-axis for soliton-induced SC generation, while the intensity and spectral bandwidth of the y-

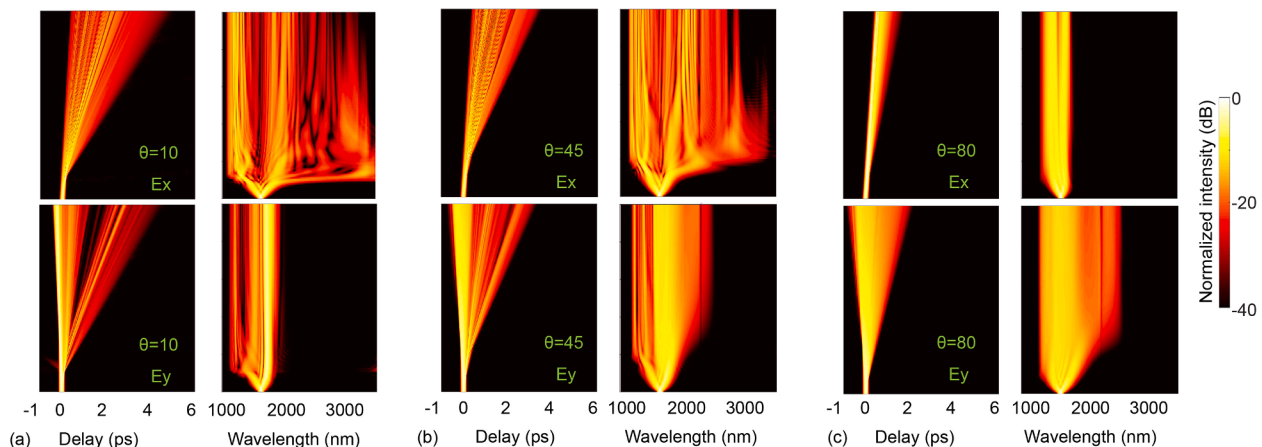


Fig. 6. Evolution of temporal and spectral profile on x- and y-axis with various input angles. (a)  $\theta = 10^\circ$ , (b)  $\theta = 45^\circ$ , and (c)  $\theta = 80^\circ$ .

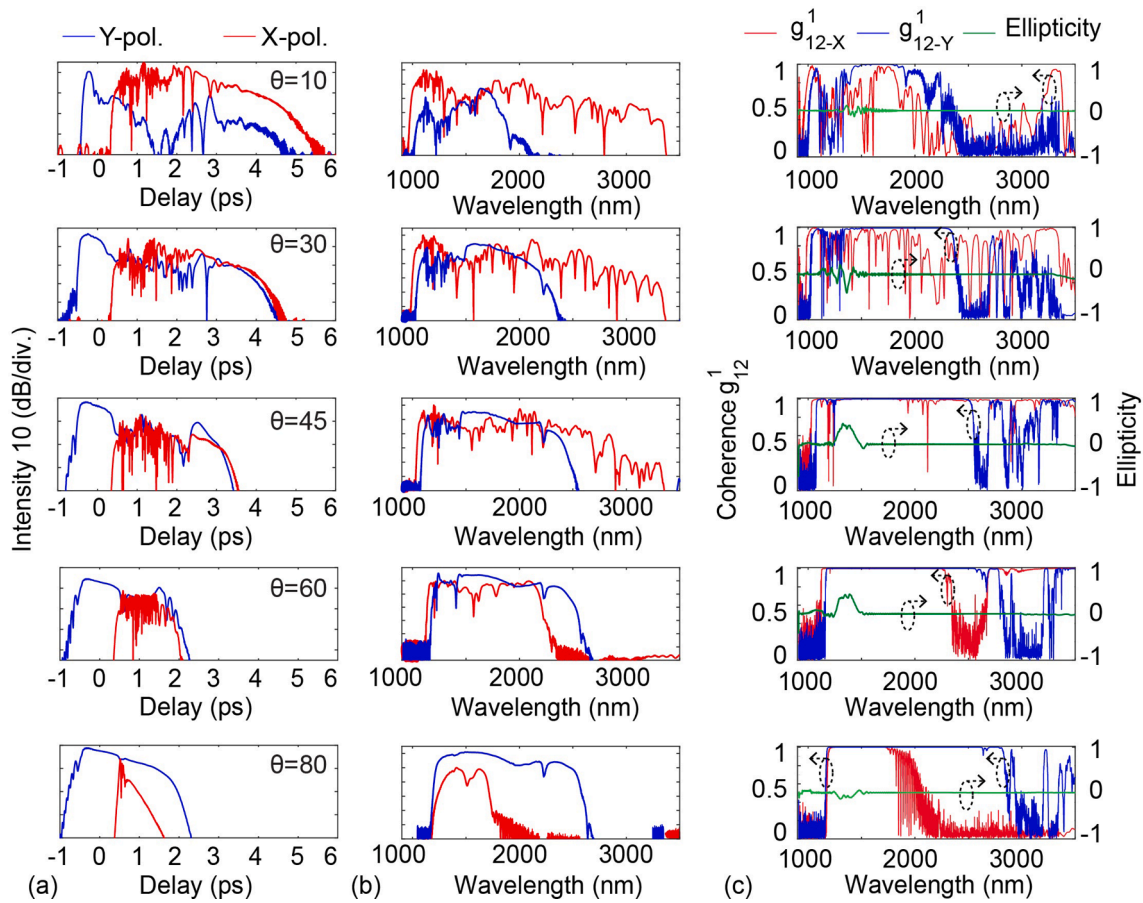


Fig. 7. SC spectrum of x- and y-component at 10 cm propagation with various input angles. (a) temporal profile, (b) SC spectrum, (c) coherence and ellipticity.

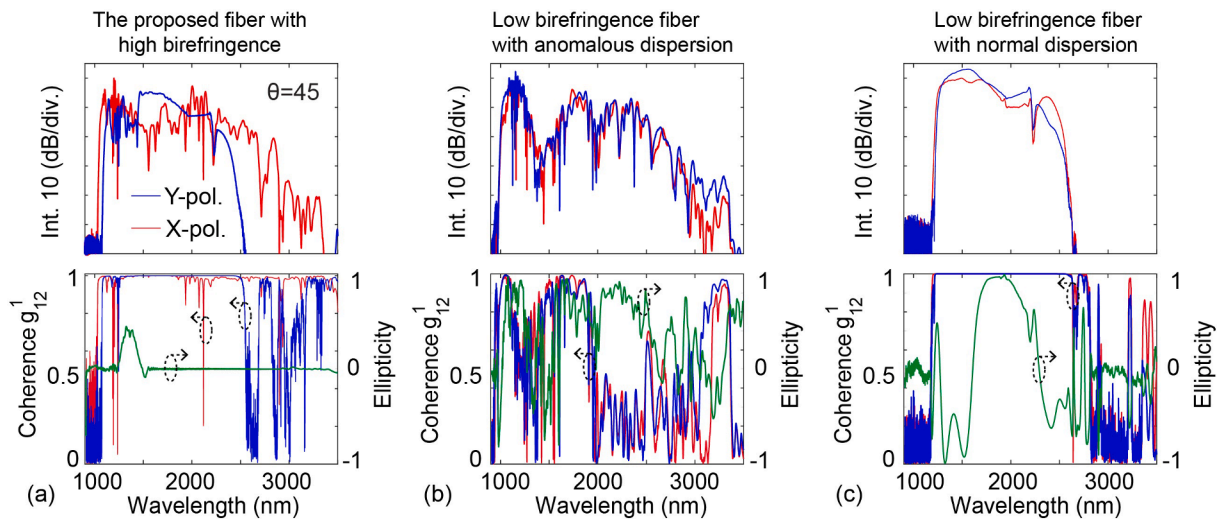


Fig. 8. (a) SC spectrum in the proposed fiber (a), low birefringence fibers with anomalous (b), and normal dispersion (c). Input laser pulses are aligned with  $\theta = 45^\circ$ .

component is increased. According to Eq. (19), reduction of input light energy leads to a decrease in the soliton number and an increase in the MI length. Consequently, the coherence smoothly improves with the increase of  $\theta$ , Fig. 7 (c). However, the increase of  $\theta$ , in turn, leads to a reduction of spectral bandwidth because the ANDi SC generation on the y-axis gets further dominant. In the other words, the proposed fiber provides a trade-off between spectral bandwidth and coherence. The simulation also shows that ellipticity does not undergo a complicated evolution, meaning that the polarization state does not change

dramatically,

In the time domain, the y-polarized mode has a higher group velocity than that of the x-polarized mode, resulting in delay time between the x- and the y-component, Fig. 7 (a). In addition, dispersion of y-polarized mode has higher absolute value than x-polarized mode over the whole investigated wavelength range, Fig. 3 (a). In such case, y-components experience further stretching out than x-components. Consequently, temporal profiles on y-components are broader than x-components for all considered input angles, Fig. 7 (a).

Fig. 8 presents a comparison of proposed fiber and low-birefringence fibers (LBFs) for input angle  $45^\circ$ . The GVM of the low birefringence fibers is assumed with a value  $\Delta\beta_1 = 10^{-3}$  ps/m, and birefringence  $B = 10^{-6}$ . We use the model in Eq. (9) to numerically simulate SC generation in the LBFs. In such model, we assume that  $b(t) \approx h_{\parallel}(t) - h_{\perp}(t)$ , and two considered LBFs have linear properties similar to those of the proposed fibers.

With input peak power of 10 kW, low birefringence fiber with anomalous dispersion provides SC spectra with bandwidth from 1000 to 3300 nm within 40 dB dynamics. The coherence in such case is low with  $\langle g_{12}^2 \rangle = 0.45$  and the ellipticity experience complex variation over the whole spectra, Fig. 8 (b). An octave-spanning ANDi SC generation is induced in the normal-dispersion LBF with high coherence, however, the ellipticity also has a complex fashion, Fig. 8 (c). Whilst, the proposed fibers provide SC generation with near-zeros ellipticity and high coherence for both x- and y-components.

## 5. Conclusion

The SC generation in high birefringence fiber infiltrated with  $\text{CS}_2$  has been studied with linearly polarized femtosecond pulses. The fiber has two modes in near IR ranges, i.e., x- and y- polarized  $\text{LP}_{01}$  in which y-polarized mode has all-normal dispersion and x-polarized mode has anomalous dispersion in near IR range with two ZDWs at 1520 nm and 2480 nm. The nonlinear dynamics, and thus, properties of SC generation in the proposed fiber depend on the input angle where either x-component or y-component becomes dominant. For input pulses polarized near the x-axis, the SC generation is induced by soliton dynamics obtaining two-octave spanning (1000 nm – 3300 nm). In contrast, the light polarized near the y-axis, the ANDi SC generation induced by SPM, OWB is dominant with octave-spanning (1200–2500 nm). The simulation also pointed out that MI is significantly dynamic to amplified vacuum noise resulting in degradation of the coherence, while PMI is suppressed because of the high birefringence of the proposed fibers. Thus, the coherence seems to smoothly improve with an increase of input angle  $\theta$ , i.e., rotate input pulses from the x-axis (slow-axis) toward the y-axis (fast-axis).

The use of liquids ( $\text{CS}_2$ ) with a high nonlinear refractive index and high transparency enables obtaining the broad bandwidth SC generation with low input peak power. The input peak power used herein (10 kW) is extremely lower than the ones for high coherence SC generation as shown in [57–59]. Therefore, the proposed fiber is possible to use for a compact SC generation system with a standard femtosecond laser as a pump source. In addition, the proposed fiber allows obtaining either broad soliton-induced SC generation or high coherence ANDi SC generation by changing the input angle. The proposed fiber, therefore, is possible to use for both applications that required broad spectral bandwidth (e.g., Mach-Zehnder interferometer, gas or liquid sensing) and applications with high pulse-to-pulse coherence (e.g., pulse compression, multibeam pump–probe technique, and temporally synchronized ultrafast amplifiers with low noise level).

## CRedit authorship contribution statement

**Lanh Chu Van:** Conceptualization, Methodology, Writing – original draft, Visualization, Investigation. **Bao Tran Le Tran:** Data curation. **Trong Dang Van:** Data curation. **Ngoc Vo Thi Minh:** Data curation. **Thuy Nguyen Thi:** . **Hong Phuong Nguyen Thi:** Writing – original draft, Visualization, Investigation. **Minh Hang Trang Nguyen:** Visualization, Investigation. **Van Thuy Hoang:** Conceptualization, Methodology, Writing – original draft, Supervision, Writing – review & editing.

## Declaration of Competing Interest

The authors declare that they have no known competing financial

interests or personal relationships that could have appeared to influence the work reported in this paper.

## Data availability

No data was used for the research described in the article.

## Acknowledgments

This research is funded by Vietnam's Ministry of Education and Training (B2023-TDV-07), and Vietnam's Ministry of Education and Training (B2021- DHH-08).

## References

- [1] S. You, H. Tu, E.J. Chaney, Y. Sun, Y. Zhao, A.J. Bower, Y.-Z. Liu, M. Marjanovic, S. Sinha, Y. Pu, S.A. Boppart, Intravital imaging by simultaneous label-free autofluorescence-multiharmonic microscopy, *Nat. Commun.* 9 (2018) 1–9, <https://doi.org/10.1038/s41467-018-04470-8>.
- [2] A.L. Gaeta, M. Lipson, T.J. Kippenberg, Photonic-chip-based frequency combs, *Nat. Photonics* 13 (2019) 158–169, <https://doi.org/10.1038/s41566-019-0358-x>.
- [3] T. Mikkonen, D. Luoma, H. Hakulinen, G. Genty, P. Vanninen, J. Toivonen, Detection of gaseous nerve agent simulants with broadband photoacoustic spectroscopy, *J. Hazard. Mater.* 440 (2022), 129851, <https://doi.org/10.1016/j.jhazmat.2022.129851>.
- [4] T. Sylvestre, E. Genier, A.N. Ghosh, P. Bowen, G. Genty, J. Troles, A. Mussot, A. C. Peacock, M. Klimczak, A.M. Heidt, J.C. Travers, O. Bang, J.M. Dudley, Recent advances in supercontinuum generation in specialty optical fibers, *J. Opt. Soc. Am. B* 38 (12) (2021) F90–F103, <https://doi.org/10.1364/JOSAB.439330>.
- [5] J.T. Woodward, A.W. Smith, C.A. Jenkins, C. Lin, S.W. Brown, K.R. Lykke, Supercontinuum sources for metrology, *Metrologia* 46 (4) (2009) S277–S282, <https://doi.org/10.1088/0026-1394/46/4/S27>.
- [6] D.R. Carlson, D.D. Hickstein, A. Lind, J.B. Olson, R.W. Fox, R.C. Brown, A. D. Ludlow, Q. Li, D. Westly, H. Leopardi, T.M. Fortier, K. Srinivasan, S.A. Diddams, S.B. Papp, Photonic-Chip Supercontinuum with Tailored Spectra for Counting Optical Frequencies, *Phys. Rev. Appl.* 8 (1) (2017), 014027, <https://doi.org/10.1103/PhysRevApplied.8.014027>.
- [7] N.M. Kearns, A.C. Jones, M.B. Kunz, R.T. Allen, J.T. Flach, M.T. Zanni, Two-dimensional white-light spectroscopy using supercontinuum from an all-normal dispersion photonic crystal fiber pumped by a 70 MHz Yb fiber oscillator, *J. Phys. Chem. A* 123 (13) (2019) 3046–3055, <https://doi.org/10.1021/acs.jpca.9b02206>.
- [8] R. R. Afano, *The Supercontinuum Laser Source*, Third Ed., Springer-Verlag, 2016.
- [9] A.M. Heidt, Pulse preserving flat-top supercontinuum generation in all-normal dispersion photonic crystal fibers, *J. Opt. Soc. Am. B* 27 (3) (2010) 550–559, <https://doi.org/10.1364/JOSAB.27.000550>.
- [10] M.L.V. Tse, P. Horak, F. Poletti, N.G.R. Broderick, J.H.V. Price, J.R. Hayes, D. J. Richardson, Supercontinuum generation at 1.06 $\mu\text{m}$  in holey fibers with dispersion flattened profiles, *Opt. Express* 14 (10) (2006) 4445–4451, <https://doi.org/10.1364/OE.14.004445>.
- [11] A.I. Adamu, M.S. Habib, C.R. Petersen, J.E.A. Lopez, B. Zhou, A. Schülzgen, M. Bache, R. Amezcua-Correa, O. Bang, C. Markos, Deep-UV to Mid-IR Supercontinuum Generation driven by Mid-IR Ultrashort Pulses in a Gas-filled Hollow-core Fiber, *Sci. Rep.* 9 (1) (2019), <https://doi.org/10.1038/s41598-019-39302-2>.
- [12] H.V. Le, V.T. Hoang, G. Stepniowski, T.L. Canh, N.V.T. Minh, R. Kasztelanica, M. Klimczak, J. Pniewski, K.X. Dinh, A.M. Heidt, R. Buczyński, Low pump power coherent supercontinuum generation in heavy metal oxide solid-core photonic crystal fibers infiltrated with carbon tetrachloride covering 930–2500 nm, *Opt. Express* 29 (24) (2021) 39586–39600, <https://doi.org/10.1364/OE.443666>.
- [13] T. Huang, K. Xia, J. Wang, H. Ren, S. Bai, P. Yang, S. Ge, L. Yang, M. Qiu, F. Yang, S. Mo, P. Zhang, R. Zhao, Y. Liu, X. Wang, S. Dai, Q. Nie, 730 mW, 2–8  $\mu\text{m}$  supercontinuum generation and the precise estimation of multi-pulse spectral evolution in the soft-glass fibers cascaded nonlinear system, *Opt. Express* 29 (25) (2021) 40934–40946, <https://doi.org/10.1364/OE.441354>.
- [14] Z. Esлами, L. Salmela, A. Filipkowski, D. Pysz, M. Klimczak, R. Buczyński, J. M. Dudley, ang G. Genty., Two octave supercontinuum generation in a non-silica graded-index multimode fiber, *Nat. Commun.* 13 (2022) 2126, <https://doi.org/10.1038/s41467-022-29776-6>.
- [15] E. Genier, S. Grelet, R.D. Engelsen, P. Bowen, P.M. Moselund, O. Bang, J. M. Dudley, T. Sylvestre, Ultra-flat, low-noise, and linearly polarized fiber supercontinuum source covering 670–1390 nm, *Opt. Lett.* 46 (8) (2021) 1820–1823, <https://doi.org/10.1364/OL.420676>.
- [16] R. Scheibinger, N.M. Lüpken, M. Chemnitz, K. Schaarschmidt, J. Kobelke, C. Fallnich, M.A. Schmidt, Higher-order mode supercontinuum generation in dispersion-engineered liquid-core fibers, *Sci. Rep.* 11 (2021) 5270, <https://doi.org/10.1038/s41598-021-84397-1>.
- [17] R. Sollaпur, D. Kartashov, M. Zürich, A. Hoffmann, T. Grigorova, G. Sauer, A. Hartung, A. Schwuchow, J. Bierlich, J. Kobelke, M. Chemnitz, M.A. Schmidt, C. Spielmann, Resonance-enhanced multi-octave supercontinuum generation in antiresonant hollow-core fibers, *Light Sci. Appl.* 6 (2017) 17124, <https://doi.org/10.1038/lsa.2017.124>.

- [18] A. Lemièrre, R. Bizot, F. Désévéday, G. Gadret, J.-C. Jules, P. Mathey, C. Aquilina, P. Béjot, F. Billard, O. Faucher, B. Kibler, F. Smektala, 1.7–18  $\mu\text{m}$  mid-infrared supercontinuum generation in a dispersion-engineered step-index chalcogenide fiber, *Results Phys.* 26 (2021), 104397, <https://doi.org/10.1016/j.rinp.2021.104397>.
- [19] V.T. Hoang, D. Dobrakowski, G. Stepniowski, R. Kasztelanic, D. Pysz, K.X. Dinh, M. Klimczak, M. Śmietana, R. Buczyński, Antiresonant fibers with single- and double-ring capillaries for optofluidic applications, *Opt. Express* 28 (2020) 32483–32498, <https://doi.org/10.1364/OE.404701>.
- [20] M. Nissen, B. Doherty, J. Hamperl, J. Kobelke, K. Weber, T. Henkel, M.A. Schmidt, UV Absorption spectroscopy in water-filled antiresonant hollow core fibers for pharmaceutical detection, *Sensors* 18 (2018) 478, <https://doi.org/10.3390/s18020478>.
- [21] L.C. Van, H.V. Le, N.D. Nguyen, N.V.T. Minh, Q.H. Dinh, V.T. Hoang, T.N. Thi, B. C. Van, “Modeling of lead-bismuth gallate glass ultra-flattened normal dispersion photonic crystal fiber infiltrated with tetrachloroethylene for high coherence mid-infrared supercontinuum generation, *Laser Phys.* 32 (2022), 055102, <https://doi.org/10.1088/1555-6611/ac599b>.
- [22] S. Liu, Y. Wang, M. Hou, J. Guo, Z. Li, P. Lu, Anti-resonant reflecting guidance in alcohol-filled hollow core photonic crystal fiber for sensing applications, *Opt. Express* 21 (2013) 31690–31697, <https://doi.org/10.1364/OE.21.031690>.
- [23] V.T. Hoang, G. Stepniowski, R. Kasztelanic, D. Pysz, V.C. Long, K.X. Dinh, M. Klimczak, R. Buczyński, Enhancement of UV-visible transmission characteristics in wet-etched hollow core anti-resonant fibers, *Opt. Express* 29 (2021) 18243–18262, <https://doi.org/10.1364/OE.426388>.
- [24] M. Chemnitz, M. Gebhardt, C. Gaida, F. Stutzki, J. Kobelke, J. Limpert, A. Tünnermann, M.A. Schmidt, Hybrid soliton dynamics in liquid-core fibres, *Nat. Commun.* 8 (2017), <https://doi.org/10.1038/s41467-017-00033-5>.
- [25] V.T. Hoang, R. Kasztelanic, G. Stepniowski, K.D. Xuan, V.C. Long, M. Trippenbach, M. Klimczak, R. Buczyński, J. Pniowski, Femtosecond supercontinuum generation around 1560 nm in hollow-core photonic crystal fibers filled with carbon tetrachloride, *Appl. Opt.* 59 (12) (2020) 3720–3725, <https://doi.org/10.1364/AO.385003>.
- [26] V.T. Hoang, R. Kasztelanic, A. Filipkowski, G. Stepniowski, D. Pysz, M. Klimczak, S. Ertman, V.C. Long, T.R. Woliński, M. Trippenbach, K.D. Xuan, M. Śmietana, R. Buczyński, Supercontinuum generation in an all-normal dispersion large core photonic crystal fiber infiltrated with carbon tetrachloride, *Opt. Mater. Express* 9 (5) (2019) 2264–2278, <https://doi.org/10.1364/OME.9.002264>.
- [27] M. Chemnitz, C. Gaida, M. Gebhardt, F. Stutzki, J. Kobelke, A. Tünnermann, J. Limpert, M.A. Schmidt, Carbon chloride-core fibers for soliton mediated supercontinuum generation, *Opt. Express* 26 (3) (2018) 3221–3235, <https://doi.org/10.1364/OE.26.003221>.
- [28] H.L. Van, V.T. Hoang, T.L. Canh, Q.H. Dinh, H.T. Nguyen, N.V.T. Minh, M. Klimczak, R. Buczyński, R. Kasztelanic, Silica-based photonic crystal fiber infiltrated with 1,2-dibromoethane for supercontinuum generation, *Appl. Opt.* 60 (2021) 7268–7278, <https://doi.org/10.1364/AO.430843>.
- [29] S. Junaid, W. Huang, R. Scheibinger, K. Schaarschmidt, H. Schneidewind, P. Paradis, M. Bernier, R. Vallée, S.-E. Stanca, G. Zieger, M.A. Schmidt, Attenuation coefficients of selected organic and inorganic solvents in the mid-infrared spectral domain, *Opt. Mater. Express* 12 (2022) 1754–1763, <https://doi.org/10.1364/OME.455405>.
- [30] M. Reichert, H. Hu, M.R. Ferdinandus, M. Seidel, P. Zhao, T.R. Ensley, D. Peceli, J. M. Reed, D.A. Fishman, S. Webster, D.J. Hagan, E.W. Van Stryland, Temporal, spectral, and polarization dependence of the nonlinear optical response of carbon disulfide, *Optica* 1 (6) (2014) 436–445, <https://doi.org/10.1364/OPTICA.1.000436>.
- [31] M. Chemnitz, R. Scheibinger, C. Gaida, M. Gebhardt, F. Stutzki, S. Pumpe, J. Kobelke, A. Tünnermann, J. Limpert, M.A. Schmidt, Thermodynamic control of soliton dynamics in liquid-core fibers, *Optica* 5 (6) (2018) 695–703, <https://doi.org/10.1364/OPTICA.5.000695>.
- [32] P. Zhao, M. Reichert, S. Benis, D.J. Hagan, E.W.V. Stryland, Temporal and polarization dependence of the nonlinear optical response of solvents, *Optica* 5 (5) (2018) 583–594, <https://doi.org/10.1364/OPTICA.5.000583>.
- [33] Y. Sato, R. Morita, M. Yamashita, Study on ultrafast dynamic behaviors of different nonlinear refractive index components in CS<sub>2</sub> using a femtosecond interferometer, *Jpn. J. Appl. Phys.* 36 (1997) 2109, <https://doi.org/10.1143/JJAP.36.2109>.
- [34] Y. Sato, R. Morita, M. Yamashita, Femtosecond optical pulse compressor using CS<sub>2</sub> liquid-core fiber with negative delayed nonlinear response, *Jpn. J. Appl. Phys.* 36 (1997) 6768, <https://doi.org/10.1143/JJAP.36.6768>.
- [35] J.M. Dudley, G. Genty, S. Coen, Supercontinuum generation in photonic crystal fiber, *Rev. Mod. Phys.* 78 (4) (2006) 1135–1184, <https://doi.org/10.1103/RevModPhys.78.1135>.
- [36] A.M. Heidt, J.S. Feehan, J.H.V. Price, T. Feurer, Limits of coherent supercontinuum generation in normal dispersion fibers, *J. Opt. Soc. Am. B* 34 (4) (2017) 764–775, <https://doi.org/10.1364/JOSAB.34.000764>.
- [37] Z. Zhu, T.G. Brown, Polarization properties of supercontinuum spectra generated in birefringent photonic crystal fibers, *J. Opt. Soc. Am. B* 21 (2) (2004) 249–257, <https://doi.org/10.1364/JOSAB.21.000249>.
- [38] I.B. Gonzalo, R.D. Engelsholm, M.P. Sørensen, O. Bang, Polarization noise places severe constraints on coherence of all-normal dispersion femtosecond supercontinuum generation, *Sci. Rep.* 8 (1) (2018) 1–13, <https://doi.org/10.1038/s41598-018-24691-7>.
- [39] E. Genier, P. Bowen, T. Sylvestre, J.M. Dudley, P. Moselund, O. Bang, Amplitude noise and coherence degradation of femtosecond supercontinuum generation in all-normal-dispersion fibers, *J. Opt. Soc. Am. B* 36 (2) (2019) A161–A167, <https://doi.org/10.1364/JOSAB.36.00A161>.
- [40] F. Xu, J. Yuan, C. Mei, B. Yan, X. Zhou, Q. Wu, K. Wang, X. Sang, C. Yu, G. Farrell, Highly coherent supercontinuum generation in a polarization-maintaining CS<sub>2</sub>-core photonic crystal fiber, *Appl. Opt.* 58 (6) (2019) 1386–1392, <https://doi.org/10.1364/AO.58.001386>.
- [41] N. Ghosh, M. Meneghetti, C.R. Petersen, O. Bang, L. Brilland, S. Venck, J. Troles, J. M. Dudley, T. Sylvestre, Chalcogenide-glass polarization-maintaining photonic crystal fiber for mid-infrared supercontinuum generation, *J. Phys. Photonics* 1 (2019), 044003, <https://doi.org/10.1088/2515-7647/ab3b1e>.
- [42] E. Tagkoudi, C.G. Amiot, G. Genty, C.-S. Brès, Extreme polarization-dependent supercontinuum generation in an uncladded silicon nitride waveguide, *Opt. Express* 29 (14) (2021) 21348–21357, <https://doi.org/10.1364/OE.430197>.
- [43] V.M. Mashinsky, V.B. Neustruev, V.V. Dvoyrin, S.A. Vasiliev, O.I. Medvedkov, I. A. Bufetov, A.V. Shubin, E.M. Dianov, A.N. Guryanov, V.F. Khopin, M.Y. Salgansky, Germania-glass-core silica-glass-cladding modified chemical-vapor deposition optical fibers: optical losses, photorefractivity, and Raman amplification, *Opt. Lett.* 29 (22) (2004) 2596–2598, <https://doi.org/10.1364/OL.29.002596>.
- [44] O.I. Medvedkov, S.A. Vasiliev, P.I. Gnusin, E.M. Dianov, Photosensitivity of optical fibers with extremely high germanium concentration, *Opt. Mater. Express* 2 (11) (2012) 1478–1489, <https://doi.org/10.1364/OME.2.001478>.
- [45] R. Buczyński, M. Klimczak, T. Stefaniuk, R. Kasztelanic, B. Siwicki, G. Stepniowski, J. Cimek, D. Pysz, R. Stepien, Optical fibers with gradient index nanostructured core, *Opt. Express* 23 (20) (2015) 25588–25596, <https://doi.org/10.1364/OE.23.025588>.
- [46] D. Pysz, I. Kujawa, R. Stepien, M. Klimczak, A. Filipkowski, M. Franczyk, L. Kociszewski, J. Buźniak, K. Haraśny, R. Buczyński, Stack and draw fabrication of soft glass microstructured fiber optics, *Bull. Pol. Acad. Sci. Tech. Sci.* 62 (2014) 667–682, <https://doi.org/10.2478/bpasts-2014-0073>.
- [47] V.T. Hoang, R. Kasztelanic, A. Anuszkiewicz, G. Stepniowski, A. Filipkowski, S. Ertman, D. Pysz, T. Woliński, K.D. Xuan, M. Klimczak, R. Buczyński, All-normal dispersion supercontinuum generation in photonic crystal fibers with large hollow cores infiltrated with toluene, *Opt. Mater. Express* 8 (11) (2018) 3568–3582, <https://doi.org/10.1364/OME.8.003568>.
- [48] M. Vieweg, T. Gissibl, S. Pricking, B. T. Kuhlmeier, D. C. Wu, B. J. Eggleton, H. Giessen, Ultrafast nonlinear optofluidics in selectively liquid-filled photonic crystal fibers, *18(24)* (2010) 25232–25240, <https://doi.org/10.1364/OE.18.025232>.
- [49] S. Kedenburg, M. Vieweg, T. Gissibl, H. Giessen, Linear refractive index and absorption measurements of nonlinear optical liquids in the visible and near-infrared spectral region, *Opt. Mater. Express* 2 (11) (2012) 1588–1611, <https://doi.org/10.1364/OME.2.001588>.
- [50] C.Z. Tan, Determination of refractive index of silica glass for infrared wavelengths by IR spectroscopy, *J. Non-Cryst. Solids* 223 (1998) 158–163, [https://doi.org/10.1016/S0022-3093\(97\)00438-9](https://doi.org/10.1016/S0022-3093(97)00438-9).
- [51] Heraeus, <https://www.heraeus.com/en/group/home/home.html>.
- [52] J.W. Fleming, Dispersion in GeO<sub>2</sub>-SiO<sub>2</sub> glasses, *Appl. Opt.* 23 (24) (1984) 4486–4493, <https://doi.org/10.1364/AO.23.004486>.
- [53] R.W. Hellwarth, Third-order optical susceptibilities of liquids and solids, *Prog. Quantum. Electron.* 5 (1977) 1–68, [https://doi.org/10.1016/0079-6727\(79\)90002-8](https://doi.org/10.1016/0079-6727(79)90002-8).
- [54] G.P. Agrawal, *Nonlinear Fiber Optics*, chapter 6, 3rd ed., Academic Press, San Diego, 2001.
- [55] L.C. Van, T.N. Thi, B.T.L. Tran, D.H. Trong, N.V.T. Minh, H.V. Le, V.T. Hoang, Multi-octave supercontinuum generation in As<sub>2</sub>Se<sub>3</sub> chalcogenide photonic crystal fiber, *Phot. Nanostruct. Fundam. Appl.* 48 (2022), 100986, <https://doi.org/10.1016/j.photonics.2021.100986>.
- [56] Y. Huang, H. Yang, S. Zhao, Y. Mao, S. Chen, Design of photonic crystal fibers with flat dispersion and three zero dispersion wavelengths for coherent supercontinuum generation in both normal and anomalous regions, *Results Phys.* 23 (2021), 104033, <https://doi.org/10.1016/j.rinp.2021.104033>.
- [57] A.M. Heidt, A. Hartung, G.W. Bosman, P. Krok, E.G. Rohwer, H. Schwoerer, H. Bartelt, Coherent octavespanning near-infrared and visible supercontinuum generation in all-normal dispersion photonic crystal fibers, *Opt. Express* 19(4) (2011) 3775–3787, <https://doi.org/10.1364/OE.19.003775>.
- [58] C. Huang, M. Liao, W. Bi, X. Li, L. Wang, T. Xue, L. Zhang, D. Chen, L. Hu, Y. Fang, W. Gao, Asterisk-shaped microstructured fiber for an octave coherent supercontinuum in a sub-picosecond region, *Opt. Lett.* 43 (3) (2018) 486–489, <https://doi.org/10.1364/OL.43.000486>.
- [59] T.L. Canh, V.T. Hoang, H.L. Van, D. Pysz, V.C. Long, T.B. Dinh, D.T. Nguyen, Q. H. Dinh, M. Klimczak, R. Kasztelanic, J. Pniowski, R. Buczyński, K.X. Dinh, Supercontinuum generation in all-normal dispersion suspended core fiber infiltrated with water, *Opt. Mater. Express* 10 (7) (2020) 1733–1748, <https://doi.org/10.1364/OME.395936>.